

Density-independent plasmons for terahertz-stable topological metamaterials

Jianfeng Wang^{1*}, Xuelei Sui^{1,2}, Wenhui Duan², Feng Liu³ and Bing Huang^{1,4*}

¹ *Beijing Computational Science Research Center, Beijing 100193, China*

² *Department of Physics and State Key Laboratory of Low-Dimensional Quantum Physics, Tsinghua University, Beijing 100084, China*

³ *Department of Materials Science and Engineering, University of Utah, Salt Lake City, Utah 84112, USA*

⁴ *Department of Physics, Beijing Normal University, Beijing 100875, China*

*Emails: bing.huang@csrc.ac.cn; wangjf@csrc.ac.cn

Abstract

To efficiently integrate cutting-edge terahertz technology into compact devices, the highly confined terahertz plasmons are attracting intensive attentions. Compared to plasmons at visible frequencies in metals, terahertz plasmons, typically in lightly doped semiconductors or graphene, are sensitive to carrier density (n) and thus have an easy tunability, which, however, leads to unstable or imprecise terahertz spectra. By deriving a simplified but universal form of plasmon frequencies, here we reveal a unified mechanism for generating unusual n -independent plasmons (DIPs) in all topological states with different dimensions. Remarkably, we predict that terahertz DIPs can be excited in 2D nodal-line and 1D nodal-point systems, confirmed by the first-principles calculations on almost all existing topological semimetals with diverse lattice symmetries. Besides of n independence, the feature of Fermi-velocity and degeneracy-factor dependences in DIPs can be applied to design topological superlattice and multi-walled carbon nanotube metamaterials for broadband terahertz spectroscopy and quantized terahertz plasmons, respectively. Surprisingly, high spatial confinement and quality factor, also insensitive to n , can be simultaneously achieved in these terahertz DIPs. Our findings pave the way to developing topological plasmonic devices for stable terahertz applications.

Bridging the gap between microwave and infrared regimes, terahertz radiation promises many cutting-edge applications in radar, imaging, biosensing, nondestructive evaluation and ultrahigh-speed communications^{1,2}. While realizing compact terahertz integrated circuits is a big challenge, terahertz plasmons, collective oscillations of electrons at terahertz frequency, provide a revolutionary way to effectively reduce the sizes of terahertz devices down to sub-wavelength scales³⁻⁸. To achieve highly confined terahertz plasmons, the extensive research has been devoted to various metamaterials, including spoof plasmon polaritons in structured metal surfaces⁷⁻¹⁰, terahertz plasmons in lightly doped semiconductors^{2,11-13} and recently developed graphene plasmons¹⁴⁻¹⁶. Compared to plasmons at visible frequency in metals, terahertz plasmons, *e.g.*, in semiconductors and graphene, are quite sensitive to the oscillation of carrier density (n)¹³⁻¹⁸, as a low n can be greatly changed by the defects¹⁷, thermal fluctuation^{2,16,19}, charge inhomogeneity²⁰, electrical gating^{14,16,18}, optical excitations²¹⁻²³ or charge transfer at interface (Fig. 1a). Consequently, their fundamental properties, such as resonance frequency, confinement and loss of terahertz plasmons^{2,16-18}, will be largely affected by the surrounding environments. Therefore, the n dependence feature leads to unfavorable terahertz applications, such as low temperature limit, high-quality sample requirements, unstable or imprecise terahertz sources and detection.

It is known that the classical plasmon frequency in conventional electronic gas (EG) has a $n^{1/2}$ dependence, while graphene plasmon shows a weaker $n^{1/4}$ power-law scaling^{14,15}. Recently, the linear band structures have been extended to a large number of topological semimetals (TSMs)^{24,25}, following the fast development of topological matter. Surprisingly, the plasmons with diverse n dependences have been found in these TSMs, even though they have a similar linear band crossing as graphene. For example, the plasmon frequency of 3D Dirac systems shows a $n^{1/3}$ scaling²⁶, while unconventional n^0 -dependent plasmons solely in mid-infrared have been found in 1D metallic carbon nanotubes (CNTs)²⁷ or 3D nodal-surface electrides²⁸. Since most of previous theories are system dependent, a unified theory to intuitively understand all these plasmonic behaviors in different electronic systems is still lacking, which significantly prevents the design of superior metamaterials for revolutionary terahertz technology and overcoming the intrinsic terahertz-unstable bottlenecks in conventional plasmonic devices.

In this article, we derive a simplified but universal form of plasmon frequencies at long-wavelength limit that can be applied to understand the collective excitations of all electronic systems with different dimensions. Significantly, a unified mechanism is revealed for generating density-*independent* plasmons (DIPs), which can be excited in some specific topological states. As demonstrated in Fig. 1a, the properties of a DIP, such as its resonance frequency or wavelength, are not affected by the changes of n , which can fundamentally overcome intrinsic terahertz-unstable bottlenecks raised by density-dependent plasmons (DDPs) in conventional systems. Importantly, we predict that the terahertz DIPs can be realized in two reduced systems: 2D nodal line and 1D nodal point. Extensive first-principles calculations are employed to confirm the DIP excitations among 22 known 2D nodal-line semimetals (NLSMs) and 1D CNTs. Besides of the n independence, the frequencies of DIPs can be tuned by Fermi velocity, substrate screening and degeneracy factor, revealing that a novel ultrastable terahertz spectrum from narrowband to broadband and a tunable quantization can be achieved in 2D superlattice and 1D multi-walled CNT metamaterials, respectively. Remarkably, stable performance with high spatial confinement and quality factor,

critical for device applications, can be simultaneously obtained for terahertz DIPs.

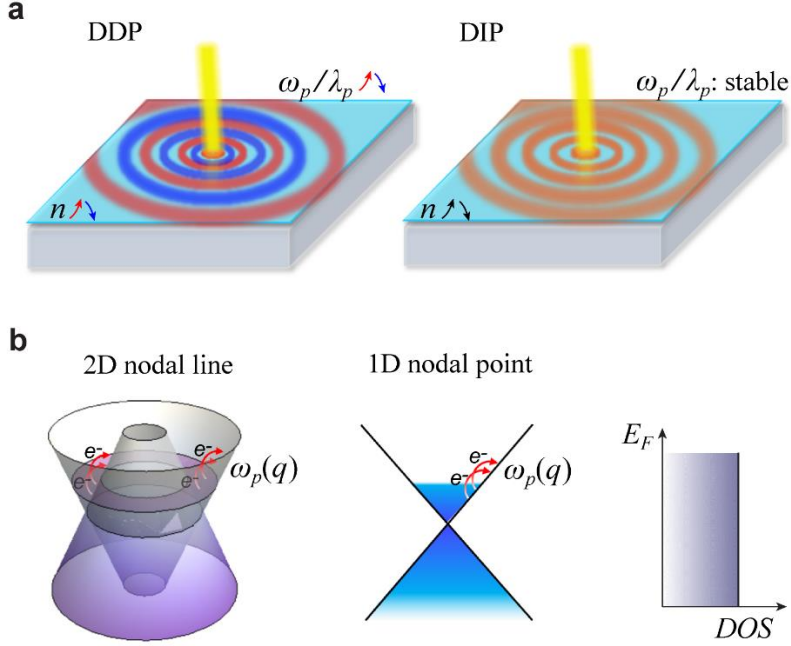


Figure 1 | DIPs and their realizations. **a**, Schematic comparison between n -dependent plasmon (DDP) and n -independent plasmon (DIP). Concentric red, blue or orange circles illustrate plasmon waves excited by electron systems (represented by the cyan plane). For an excited DDP, its resonance frequency (ω_p) or wavelength (λ_p) is sensitive to the oscillation of n . When increasing (red arrow) or decreasing (blue arrow) n , the ω_p or λ_p of a DDP will increase (red circles) or decrease (blue circles) correspondingly. While the properties (ω_p or λ_p) of a DIP (orange circles) are stable against the changes of n . **b**, Linear band structures of 2D nodal line and 1D nodal point, and their constant DOS versus E_F . Collective DIPs are labeled schematically by red arrows.

A unified mechanism for DIPs

The plasmon excitation can be determined by the dynamical dielectric function $\epsilon(\mathbf{q}, \omega) = 1 - V(\mathbf{q})\Pi(\mathbf{q}, \omega)$, where $V(\mathbf{q})$ is dimension-related Coulomb interaction in the wave vector space, and $\Pi(\mathbf{q}, \omega)$ is the irreducible polarizability function (see Methods section). As a function of Fermi energy (E_F), the key polarizability is usually n -dependent. Under RPA and long-wavelength limit, the D -dimensional noninteracting irreducible polarizability near E_F can be approximated by Taylor's first-order expansion,

$$\Pi(\mathbf{q}, \omega) \approx \frac{g}{(2\pi)^D} \int d^D \mathbf{k} \frac{\partial n_F}{\partial E} \left(\frac{\partial E}{\partial k} \right)^2 \left(\frac{q}{\hbar\omega} \right)^2, \quad (1)$$

where n_F is the Fermi-Dirac distribution function, and g is the degeneracy factor including degeneracies of spin, valley and conducting channel. Around $T=0$ K, we derive, by solving the zeros of dielectric function, a simplified but general form of the plasmon frequency,

$$\omega_p \approx \rho(E_F)^{1/2} v_F V(\mathbf{q})^{1/2} q, \quad (2)$$

where $\rho(E_F)$ is the density of states (DOS) of electrons, and $v_F = \hbar^{-1}(\partial E/\partial k)_F$ is the Fermi velocity. Equation (2), one of our key results, is universal for all dimensional solids, which reveals the most essential elements related to plasmons. Obviously, it shows that, besides of $V(\mathbf{q})$, ω_p is mostly determined by DOS and v_F .

Now we can shed light on the nature of n dependence of plasmons for all known systems. For the conventional EGs in metals or doped semiconductors exhibiting a parabolic energy dispersion $E(\mathbf{k}) = \hbar^2 k^2 / 2m$, their v_F are E_F - (or n -) dependent. As listed in Table 1, the DOS of conventional EGs is related to their dimensions (see Supplementary Section I). Based on Eq. (2), ω_p of all conventional EGs has a well-known $n^{1/2}$ power-law scaling (Table 1). While all the TSMs have a linear band dispersion $E(\mathbf{k}) = \hbar v_F k$, whose v_F is a constant. In terms of the dimensionality of band crossings, TSMs can be classified into nodal point, nodal line and nodal surface^{24,25,29}. As demonstrated in Table 1, the ω_p of TSMs has different scalings, solely dependent on their DOS.

As shown in the right column of Table 1, we have derived rigorously the analytical expressions of ω_p for all systems with different dimensions (see Methods section and Supplementary Section II), confirming that Eq. (2) could accurately capture the power-law scaling of ω_p , *e.g.*, the $n^{1/4}$ and $n^{1/3}$ DDPs are well reproduced for 2D (*e.g.*, graphene) and 3D nodal-point (*e.g.*, Dirac semimetal) systems, respectively. Interestingly, a plasmon with the same n -dependent scaling as graphene also appears in 3D nodal-line systems but it has a different anisotropy. In fact, all the analytical expressions in Table 1 can be obtained from Eq. (2) with only a difference of dimensionless coefficient.

Based on Eq. (2), we can reveal a unified mechanism for realizing a DIP, which needs to meet two general criteria: (i) a constant DOS near E_F ; (ii) a constant v_F . While (ii) can be naturally achieved in the linear band dispersion region of a TSM, (i) is the key criterion for achieving a DIP. After systematic derivations (see Supplementary Sections I and II), we conclude that the constant DOS and the resulting DIPs can solely exist in the following TSM states: 3D nodal surface, 2D nodal line and 1D nodal point, as listed in Table 1. It is noted that the plasmons occurred in wide parabolic quantum wells^{30,31} can be independent of the electron numbers (not electron density) under certain conditions, which is fundamentally different from our DIPs. We illustrate the constant DOS of 2D nodal line and 1D nodal point in Fig. 1b. At long-wavelength limit, the excitation process mainly occurs near E_F . For 2D nodal line, all states involved are in the vicinity of two rings, and the total numbers of their sum will keep a constant when changing E_F (Fig. 1b). For 1D nodal point, the total states in the excitations are at two points, and their numbers are also unchanged (Fig. 1b). It is noted that all systems are supposed to behave as Fermi liquids, although 1D metallic electrons may also be considered as a Luttinger liquid³².

As listed in Table 1, the analytical expressions clearly demonstrate the nature of DIPs in 3D nodal surface, 2D nodal line and 1D nodal point. Besides of the n independence, their ω_p are determined by some other physical quantities, *i.e.*, Fermi velocity v_F , degeneracy factor g and size of degenerate node (k_0 for line node, and S for surface node), giving the tunable factors. Interestingly, the ω_p of all TSMs is manifestly quantum with an explicit “ \hbar ”, in contrast to the classical plasmons of conventional EGs²⁶. In addition, the plasmon dispersion is related to the dimension, which is important for the size effect and spatial compression of plasmons. In order to realize the terahertz metamaterials, we focus on 2D nodal-line and 1D nodal-point systems (the high DOS prevents the realization of terahertz ω_p in 3D nodal surface²⁸). The background dielectric constant (κ) of these two systems is determined by the surrounding media, providing another tunable factor of ω_p .

Table 1 | Plasmon frequencies in all dimensions at long-wavelength limit

Systems	ρ	$\rho^{1/2} \cdot v_F$	analytical expression of ω_p
conventional EG	$E_F^{1/2} (n^{1/3})$	$n^{1/2}$	$\sqrt{\frac{4\pi e^2 n}{\kappa m}}$, (3.1)
3D	nodal point	$E_F^2 (n^{2/3})$	$\sqrt{\frac{e^2 v_F}{\kappa \hbar}} \left(\frac{32\pi g}{3}\right)^{1/6} n^{1/3}$, (3.2)
	nodal line	$E_F (n^{1/2})$	$\sqrt{\frac{2\pi e^2 v_F}{\kappa \hbar}} (1 + \sin^2 \theta) (g\pi k_0 n)^{1/4}$, (3.3)
	nodal surface	$E_F^0 (n^0)$	$\sqrt{\frac{g e^2 v_F S \cos^2 \theta}{\pi^2 \kappa \hbar}}$, (3.4)
conventional EG	$E_F^0 (n^0)$	$n^{1/2}$	$\sqrt{\frac{2\pi e^2 n}{\kappa m}} q^{1/2}$, (3.5)
2D	nodal point	$E_F (n^{1/2})$	$\sqrt{\frac{e^2 v_F}{\kappa \hbar}} (g\pi n)^{1/4} q^{1/2}$, (3.6)
	nodal line	$E_F^0 (n^0)$	$\sqrt{\frac{g e^2 v_F k_0}{\kappa \hbar}} q^{1/2}$, (3.7)
conventional EG	$E_F^{-1/2} (n^{-1})$	$n^{1/2}$	$\sqrt{\frac{2e^2 n}{\kappa m}} q \sqrt{ \ln(qa) }$, (3.8)
1D	nodal point	$E_F^0 (n^0)$	$\sqrt{\frac{2g e^2 v_F}{\pi \kappa \hbar}} q \sqrt{ \ln(qa) }$. (3.9)

Physical quantities: DOS ρ , Fermi velocity v_F , electron charge e , effective mass m , background dielectric constant κ , degeneracy factor g , size of line (surface) node k_0 (S), and lateral confinement size of 1D electron system a . See Supplementary Information for the detailed derivations. Systems exhibiting DIPs are highlighted by red colors. All conventional EGs have a parabolic dispersion, while all TSMs have a linear dispersion.

Terahertz DIPs in 2D NLSMs

The 2D NLSMs, having a symmetry-protected crossing between conduction and valence bands along a 1D loop in the Brillouin zone (BZ), attract intensive interests, due to their potential applications in quantum devices. Until now, the 2D NLSMs includes at least 22 compounds with a wide range of lattice symmetries, *e.g.*, honeycomb lattice CuSe³³, AgTe³⁴ and *h*-B₂O³⁵, honeycomb-Kagome lattice Hg₃As₂³⁶, honeycomb-triangular lattice Cu₂Si³⁷, Lieb lattice Be₂C³⁸, and tetragonal lattice X_2Y (X =Ca,Sr,Ba; Y =As,Sb,Bi)³⁹, etc. These 2D nodal lines are protected by (glide) mirror symmetries. Importantly, all these NLSMs can exhibit the terahertz DIP feature, confirming our unified theory in 2D systems. Here, we take the experimentally synthesized Cu₂Si as an example to demonstrate its DIP excitations, leaving the results of other 21 compounds in Supplementary Section IV.

As shown in Fig. 2a, the monolayer Cu₂Si is composed of a honeycomb Cu lattice and a triangular Si lattice. All Cu and Si atoms are coplaner and thus a mirror reflection symmetry with respect to xy plane (M_z) is kept. First, we illustrate the electronic properties of free-standing Cu₂Si. The calculated band structure without spin-orbit coupling (SOC) is shown in Fig. 2b. Two band crossings between one conduction band and two valence bands occur along Γ - M and Γ - K lines. Actually, the band crossings take place along two loops in the 2D BZ, as shown in the 2D band plot (Fig. 2c).

Thus, two concentric nodal lines are formed centred around the Γ point. With opposite eigenstate parities of M_z for the conduction and two valence bands³⁷, the two nodal lines are protected by mirror reflection symmetry (Supplementary Fig. S1). Remarkably, the nearly constant DOS maintains over a large energy range near the Fermi level (Fig. 2b), which is the key condition for the formation of DIP excitations in a TSM. After including SOC effect, the degeneracy of 2D nodal line is slightly lifted with the appearance of a negligible gap³⁷ (Supplementary Fig. S1).

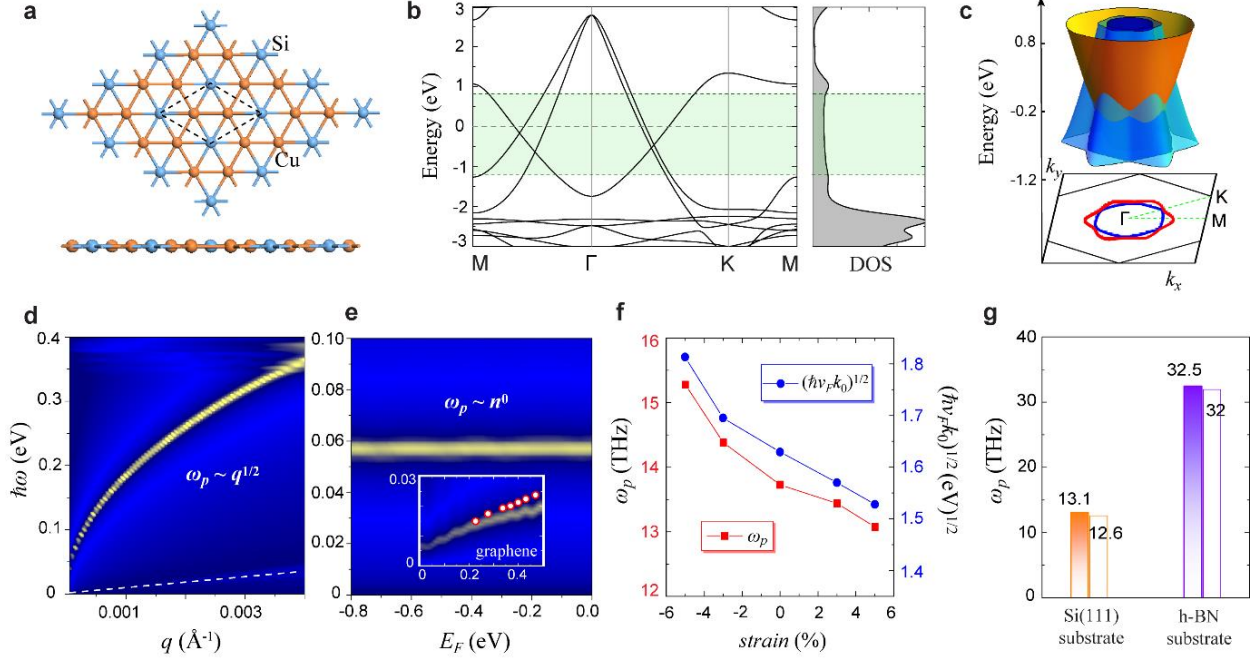


Figure 2 | DIP in 2D NLSM Cu₂Si. **a**, Top and side views of monolayer Cu₂Si. Black rhombus depicts primitive cell. **b**, Calculated band structure and DOS (without SOC) for Cu₂Si. Fermi level is set to zero. **c**, 3D plot of 2D bands in the energy range from -1.2 to 0.8 eV (green region in **b**). Band crossings between conduction and two valence bands are projected to the 2D BZ (red and blue loops). **d**, EELS as a function of frequency and wave vector. White-dashed line denotes the upper edge $\hbar v_F q$ of intraband particle-hole continuum. **e**, EELS as a function of frequency and Fermi energy ($q = 0.0001 \text{ \AA}^{-1}$). Inset: EELS of graphene plasmon with the same calculation parameters as Cu₂Si. Experimental data of graphene¹⁴ are marked as red circles (their brightness indicates the plasmon oscillation strength). **f**, Calculated plasmon frequency and related physical quantities obtained from band structures under strain. **g**, Plasmon frequency with two different substrates. Solid columns: numerical results from first principles; hollow columns: analytical results calculated from Formula (3.7) in Table 1.

Next, we discuss the plasmon excitation of Cu₂Si. The dynamical dielectric function $\epsilon(\mathbf{q}, \omega)$ is numerically calculated with 2D Coulomb interaction $V(q)$ and a background dielectric screening of SiO₂/Si substrate (see Methods section). An electron energy loss spectrum (EELS) is given by the imaginary part of the inverse of $\epsilon(\mathbf{q}, \omega)$, whose broadened peaks indicate the plasmons²⁸. As shown in Fig. 2d, a 2D plasmon dispersion ($\omega_p \sim q^{1/2}$) is demonstrated; similar to the case of graphene plasmons⁴⁰, it lies above the region of intraband electron-hole continuum, indicating that the direct Landau damping is forbidden. Using a typical micron wavelength ($q = 0.0001 \text{ \AA}^{-1}$), we plot the EELS as a function of ω_p and E_F (corresponding to n) in Fig. 2e; it shows a clear n -independent feature ($\omega_p \sim n^0$), confirming the existence of DIP. As a comparison, the inset of Fig. 2e shows calculated results of graphene plasmon, agreeing well with the experimental data (red

circles)¹⁴; the well-known $\omega_p \sim E_F^{1/2}$ ($\propto n^{1/4}$) relationship of graphene plasmon is revealed. In addition, the plasmon of Cu₂Si has a significantly larger oscillation strength than that of graphene, because of the higher DOS.

At a fixed micron wavelength, the plasmon of Cu₂Si stabilizes at a certain THz frequency with high intensity (Fig. 2e). As shown in Formula (3.7) in Table 1, the ω_p of 2D nodal line can be tuned by changing Fermi velocity v_F and line node size k_0 , which is demonstrated by the strain effect on Cu₂Si (Fig. 2f and Supplementary Fig. S2). The calculated ω_p and $(v_F k_0)^{1/2}$ have a consistent trend, confirming the validity of Formula (3.7). It notes that strain has a small effect on the change of v_F and k_0 ; consequently, $\sim 5\%$ strain can slightly induce a ~ 2 THz change of ω_p . On the other hand, ω_p is also sensitive to the background dielectric constant κ [Formula (3.7)]. As shown in Fig. 2g, we further compare the ω_p of Cu₂Si on two substrates, *i.e.*, Si(111) and *h*-BN, with quite different κ . Importantly, the nodal lines can survive on both substrates (see Supplementary Fig. S3). Interestingly, a 3-fold frequency change, from terahertz to mid-infrared, can be achieved by simply changing the underneath substrate of Cu₂Si.

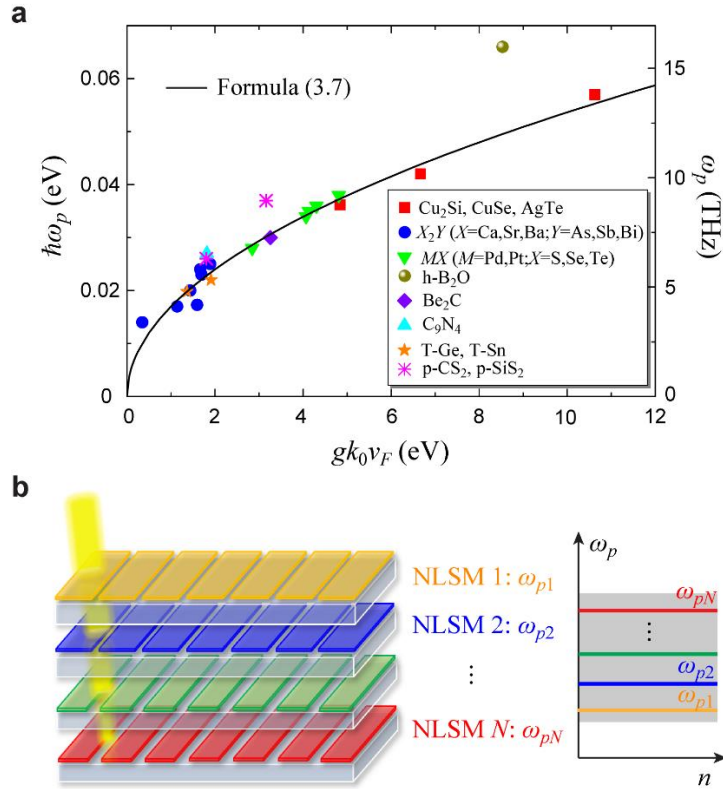


Figure 3 | DIPS in 2D NLSM metamaterials for ultrastable and broadband terahertz spectroscopy. **a**, Plasmon frequency as a function of gk_0v_F for 22 2D NLSMs, where $q = 0.0001 \text{ \AA}^{-1}$ and SiO₂/Si substrate are adopted (see Methods section). 22 colored points: numerical results obtained from first principles; black curve: analytical results obtained from Formula (3.7). **b**, Van der Waals heterostructures or grating superlattice of 2D NLSMs for ultrastable terahertz spectroscopy. For grating superlattice, transparent substrates are needed.

A broadband terahertz spectroscopy in 2D NLSM metamaterials

The intrinsic properties of nodal line (e.g., v_F and k_0) are material-dependent, indicating that a

broad range of DIPs with different ω_p may be achieved by the choice of different TSMs. Indeed, the DIP features are not only confirmed in all other NLSMs (see Supplementary Figs. S4–S11), but also exhibit a broad range from 4 THz (in Ca_2As) to 16 THz (in $h\text{-B}_2\text{O}$) (see Fig. 3a and Supplementary Table S2). Once again, the ω_p obtained from Formula (3.7) fit well with the first-principles results independent of their diverse lattice symmetries, except for the case of $h\text{-B}_2\text{O}$, which is due to the strong anisotropy of its nodal line³⁵ (see Supplementary Fig. S7).

Recently, the development of 2D van der Waals (vdW) heterostructures enables manipulating crystals for exploration of physics not observable in conventional materials^{41,42}. Employing the heterostructures (or superlattice) of 2D NLSMs, here a novel ultrastable terahertz metamaterial device can be proposed, as drawn in Fig. 3b. For vdW stackings of 2D NLSMs, a compensation momentum is necessary for incident light, which can be realized in the scattering-type scanning near-field optical microscopy (s-SNOM) technology^{16,27}. The 2D NLSMs can also be fabricated in micro-ribbon arrays on transparent substrates¹⁴; thus a grating superlattice can be well designed by stacking them layer by layer (Fig. 3b). Determined by the selections of fabricated NLSMs, ribbon/gap width and even substrates, multiple terahertz-frequency plasmons can be simultaneously excited. For instance, one can adopt the same or different materials/pattern periods for fabrications. Thus, a terahertz spectroscopy from narrowband to broadband can be achieved. Most importantly, the spectroscopy in such device could be ultrastable under the variable environments against charge doping. Our proposed device can be used as an ultrastable terahertz signal amplifier or an ultrastable terahertz sensor, which could selectively output or detect multi-band terahertz waves.

Terahertz DIPs in 1D CNTs

The nodal-point semimetals have been widely studied, *e.g.*, Dirac points in 2D graphene or 3D Na_3Bi ²⁵. To confirm our DIP model in 1D nodal-point systems [Formula (3.9) in Table 1], armchair CNTs have been selected as typical examples, as they are known as 1D Dirac-point semimetals⁴³.

The structure and 1D Dirac bands of armchair CNTs are shown in Supplementary Fig. S12. The calculations of (5,5), (10,10) and (15,15) nanotubes reveal that the v_F of Dirac electrons are almost independent of their tube diameters a and all of them have a constant DOS near the Fermi level (Supplementary Fig. S12). Using 1D Coulomb interaction and a BN substrate dielectric screening (see Methods section), the $\epsilon(\mathbf{q}, \omega)$ and EELS of these CNTs can be obtained. As shown in Fig. 4a, the plasmon dispersion of (5,5) nanotube demonstrates a typical 1D feature ($\omega \sim |q|$ at long wavelength). It also lies above the region of intraband electron-hole continuum without direct Landau damping. With a micron wavelength ($q = 0.0001 \text{ \AA}^{-1}$), the EELS as a function of ω_p and E_F (corresponding to n) for (5,5) and (10,10) nanotubes is calculated, as shown in Fig. 4b. Remarkably, the terahertz DIP feature ($\omega_p \sim n^0$) is revealed for both CNTs, and the ω_p calculated from first principles are consistent with the analytical results (red-dashed lines in Fig. 4b). Moreover, the ω_p of CNTs are almost a -independent, as a result of the weak a -dependent v_F , *i.e.*, there is only a weak logarithm dependence on the diameter of CNTs⁴⁴ [see Formula (3.9)]. Interestingly, the recent experimental observations on metallic nanotubes with different diameters confirm the existence of mid-infrared DIPs²⁷. Our results are in good agreement with the experimental measurements (red triangles in Fig. 4a), also reflecting the weak a dependence.

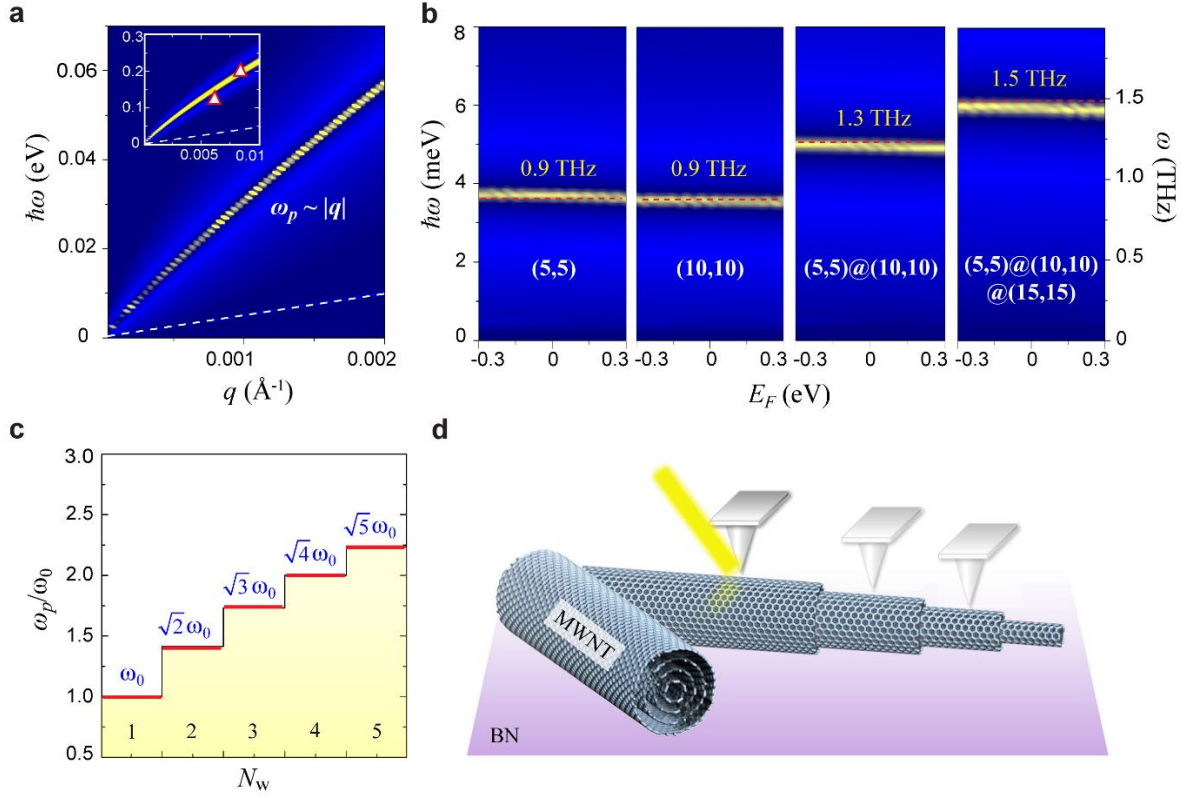


Figure 4 | Terahertz DIPs in 1D metallic CNTs and their quantization. **a**, EELS as a function of frequency and wave vector. White-dashed line denotes the upper edge $\hbar v_F q$ of intraband particle-hole continuum. Inset: EELS at a large scale of wave vector. Red triangles: experimental data adopted from ref. 27. **b**, EELS as a function of frequency and Fermi energy for two different single-, (5,5)@(10,10) double- and (5,5)@(10,10)@(15,15) triple-walled nanotubes ($q = 0.0001 \text{ \AA}^{-1}$). Red-dashed lines: analytical results from Formula (3.9) in Table 1. **c**, A quantized DIP frequency as a function of the number of walls (N_w) in multi-walled nanotubes (MWNT). **d**, Schematic plot of 1D MWNT metamaterial for an ultrastable terahertz spectroscopy with tunable and quantized frequencies.

Quantized terahertz plasmons in 1D CNT metamaterials

In terms of Formula (3.9), the weak a dependence indicates that ω_p of CNTs is mostly determined by the degeneracy factor g . In multi-walled nanotubes (MWNT), the Dirac points could maintain due to the weak vdW interactions between the individual tubes (Supplementary Fig. S12); meanwhile, the long-range Coulomb interactions make conducting channels of electrons determined by the number of walls (N_w). Thus, we propose that a quantized terahertz ω_p may be achieved in MWNT metamaterials. As shown in Fig. 4b, the calculated plasmon excitations of (5,5)@(10,10) double-walled nanotubes and (5,5)@(10,10)@(15,15) triple-walled nanotubes are demonstrated. Interestingly, besides the DIP feature, the ω_p of MWNT can exhibit a clear quantized plateau as a function of N_w , as shown in Fig. 4c. It notes that a similar quantization of propagation velocity has been observed in single-walled CNT bundles²⁷, explained by a many-body Luttinger-liquid theory. Importantly, differing from the previous theory²⁷, the emergence of quantized ω_p comes naturally from our unified DIP theory in 1D system [Formula (3.9)]. Therefore, a quantized manipulation of ultrastable terahertz plasmons using a series of MWNT can be well designed (Fig. 4d), *e.g.*, discrete frequencies or wavelengths can be excited at different thickness of a telescoping MWNT. Meanwhile, a s-SNOM technology may be needed^{16,27}.

Spatial confinement and lifetime of terahertz DIPs

As two important figures of merit for plasmonics, spatial confinement and quality factor are also calculated for the DIPs in 2D NLSMs and 1D CNTs, in comparison to graphene plasmon (see Fig. 5 and Supplementary Fig. S13). The spatial confinement, defined as the ratio of free-space light wavelength and plasmon wavelength (λ_0/λ_p), is found to be related to the dimensions: with increasing the ω_p , it can be enhanced for 2D systems but almost unchanged for 1D plasmons, consistent with the theoretical derivations (see Fig. 5a and Supplementary Section VII). Strong confinement effect is available for terahertz DIPs, *e.g.*, in (5,5) CNTs and Ca₂As (Fig. 5a), which is critical for the design of compact devices. The quality factor (Q), measuring the number of oscillating cycles a plasmon can propagate, is related to the plasmonic damping rate or lifetime. Due to the forbidden or weak direct Landau damping, the phonon-assisted damping rate of plasmons is solely considered (see Methods section). The calculated lifetimes (τ_p) can reach tens of picoseconds at low ω_p but reduce rapidly when ω_p increases to the frequency of optical phonons (Fig. 5b).

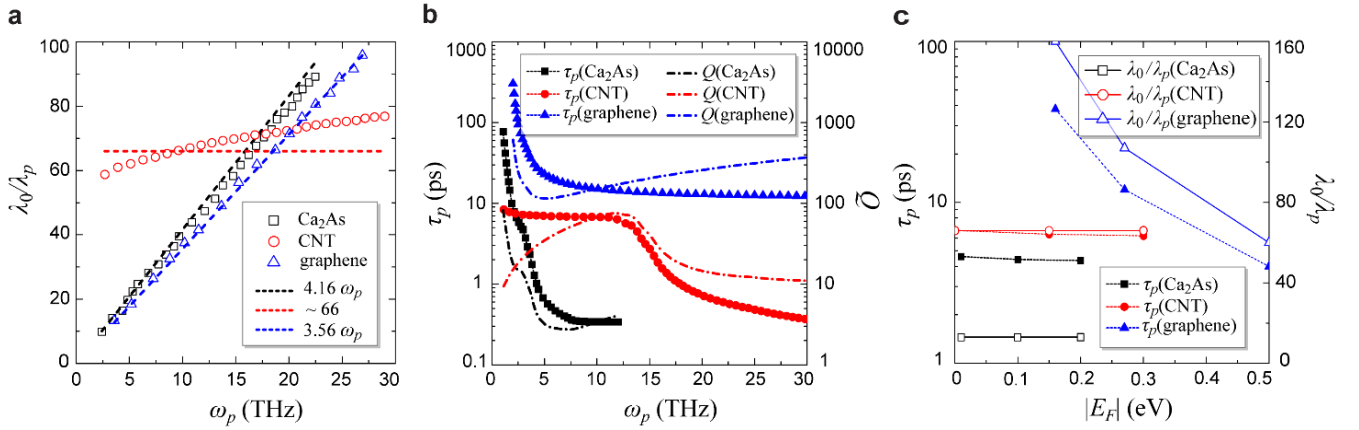


Figure 5 | Spatial confinement and lifetime of DIPs. **a**, Spatial confinement (λ_0/λ_p) as a function of ω_p for Ca₂As, (5,5) CNT and graphene. The dashed lines are theoretically derived λ_0/λ_p for the three systems (see Supplementary Section VII). $E_F = 0.27$ eV is adopted for graphene, in order to compare with experiment¹⁶. **b**, Lifetime (τ_p) and quality factor (Q) as functions of ω_p for Ca₂As, CNT and graphene. **c**, λ_0/λ_p and τ_p as functions of $|E_F|$ for Ca₂As, CNT and graphene. The ω_p is fixed at 3, 10 and 30 THz for Ca₂As, CNT and graphene, respectively.

Usually, strong spatial confinement of a plasmon is achieved at the expense of a low quality factor for metals. Remarkably, the calculated mid-infrared graphene plasmon (*e.g.*, at 30 THz) could simultaneously exhibit extraordinary spatial confinement ($\lambda_0/\lambda_p \sim 105$) and high quality factor ($Q \sim 360$), consistent with the experimental observations¹⁶. Interestingly, the simultaneous high spatial confinement and quality factor can be also achieved in terahertz DIPs, *e.g.*, $\lambda_0/\lambda_p \sim 13$ (66), $Q \sim 15$ (67) for plasmon in Ca₂As (CNT) at 3 (10) THz. As shown in Fig. 5c, the performance (λ_0/λ_p and τ_p) of graphene plasmons can be greatly affected by the charge doping, which is also demonstrated in a recent experiment¹⁸. However, for terahertz DIPs, these figures of merit are robust against the change of n (Fig. 5c), revealing that the n -independent feature of DIPs also benefits their device performance.

Discussion and Conclusion

For 2D NLSMs, some of them have been synthesized on metal substrates^{33,34,37}. Although the mirror reflection symmetry is broken considering the different media of vacuum and substrate, the nodal lines survive due to the weak substrate-overlayer interactions³⁷. Because of the significantly different excitation regions of ω_p in these NLSMs (terahertz) and their metal substrates (ultraviolet), we expect that the novel DIPs are ready to be detected in the experiments. It is also expected that they can further be deposited on insulating substrates (such as SiO₂/Si or BN) by the transfer technique⁴² for better optical measurements, where near-field optical microscope^{16,27} or lithography and etching technologies¹⁴ may need to be adopted. Meanwhile, some other 2D NLSMs are expected to be synthesized or exfoliated from their bulk materials. For 1D nodal-point TSMs, the large-scale, high-quality CNTs can be synthesized in the experiments⁴⁵.

In conclusion, we reveal a unified mechanism for generating unconventional DIPs in some specific topological systems, which can benefit the stable functionalities of plasmons in changeable environments especially for the stable terahertz applications. Our study has significant impacts in multiple fields: First, the unified mechanism we revealed not only could deepen our understandings on plasmons, but also provide a guide to the experimental realizations of unconventional DIPs in a series of topological matters. Second, combining with a large number of TSMs, a completely new type of terahertz plasmons are ready to be applied in compact terahertz devices with high stability and precision, such as ultrastable signal amplification and accurate detection. Especially, with the developments of vdW heterostructures^{41,42}, new concepts of terahertz topological metamaterials can be designed to achieve a terahertz-stable spectroscopy from narrowband to broadband or a quantized manipulation of terahertz frequencies. Therefore, our work paves the way to developing exotic plasmonic applications in nanophotonic and nanophotovoltaic devices, which may potentially open a new field for terahertz-stable plasmonics and related technologies.

Methods

First-principles calculations

The first-principles calculations are performed using the Vienna ab initio simulation package⁴⁶ within the projector augmented wave method⁴⁷ and the generalized gradient approximation of the Perdew-Burke-Ernzerhof⁴⁸ exchange-correlation functional. The Γ -centered k -point meshes are adopted. Fixing the crystal symmetry, the structures from experiments or literatures are relaxed until the residual forces on each atom is less than 0.01 eV/Å. The thickness of vacuum is taken to be 18 Å, which is adequate to simulate 2D or 1D materials. Cu₂Si has a lattice constant of 4.123 Å, and the crystal structures of other materials can be found in Supplementary Information. Spin-orbit coupling (SOC) is also considered in part of our calculations. A tight-binding (TB) Hamiltonian based on the maximally localized Wannier functions (MLWF)⁴⁹ is constructed to get the energy eigenvalues and eigenstates for further dielectric function calculations.

Plasmon calculations

The plasmon excitation can be determined by

$$\epsilon(\mathbf{q}, \omega) = 1 - V(q)\Pi(\mathbf{q}, \omega) = 0, \quad (4)$$

where $\epsilon(\mathbf{q}, \omega)$, a function of the wave vector \mathbf{q} and frequency ω , is the dynamical dielectric function. $V(q)$ is the D -dimensional Coulomb interaction in the wave vector space²⁶

$$V(q) = \begin{cases} 4\pi e^2/\kappa q^2, (D = 3) \\ 2\pi e^2/\kappa q, (D = 2) \\ 2e^2|\ln(qa)|/\kappa, (D = 1) \end{cases} \quad (5)$$

$\kappa = 4\pi\epsilon_0\epsilon_r$ is the background dielectric constant, where ϵ_0 and ϵ_r are the vacuum and background relative dielectric constants, respectively. $\Pi(\mathbf{q}, \omega)$ is the irreducible polarizability function. Under RPA and long-wavelength limit ($q \rightarrow 0$), the plasmon frequency in a D -dimensional electron system can be determined by a noninteracting irreducible polarizability^{26,28}

$$\Pi(\mathbf{q}, \omega) = \frac{g}{(2\pi)^D} \int d^D \mathbf{k} \sum_{l,l'} \frac{n_F(E_{\mathbf{k},l}) - n_F(E_{\mathbf{k}+\mathbf{q},l'})}{\hbar\omega + E_{\mathbf{k},l} - E_{\mathbf{k}+\mathbf{q},l'} + i\eta} F_{ll'}(\mathbf{k}, \mathbf{q}), \quad (6)$$

in which n_F is the Fermi-Dirac distribution function, and $F_{ll'}(\mathbf{k}, \mathbf{q})$ is the overlap form factor $|\langle \mathbf{k} + \mathbf{q}, l' | e^{i\mathbf{q}\cdot\mathbf{r}} | \mathbf{k}, l \rangle|^2$, with $|\mathbf{k}, l\rangle$ and $E_{\mathbf{k},l}$ the eigenstate and energy dispersion respectively. The factor g in Eq. (6) is the degeneracy factor including degeneracies of spin, valley and conducting channel, and η is related to the electron lifetime due to the damping. The zeros of complex dielectric function signify a self-sustaining collective mode and give the plasmon frequency.

Numerical calculations: The energy eigenvalues and eigenstates in Eq. (6) are obtained from the TB Hamiltonian of MLWF. The integral is over the first BZ, where a temperature of 300 K in the Fermi-Dirac distribution function and an infinitesimal broadening $\eta = 1$ meV are used. Considering the spin degree of freedom, the degeneracy factor g is set to 2 in the numerical calculations of all systems; while in theoretically derived formula in Table 1, g should be adopted as 4 for Cu₂Si, CuSe and AgTe, because of the two nodal lines in these three TSMs, and 4 (6) for double-walled nanotubes (triple-walled nanotubes). For $V(q)$, the relative dielectric constant is determined by $\epsilon_r = (\epsilon_0 + \epsilon_{\text{sub}})/2$ for 2D and 1D systems, representing the effective dielectric function of environments (vacuum and substrate). For a SiO₂/Si substrate, $\epsilon_r = 5$ ¹⁴; for a BN substrate, $\epsilon_r = 1$ ²⁷. In the 1D Coulomb interaction, a is lateral confinement size of 1D electron system, *e.g.*, the diameter of nanotubes. When studying the density dependence of plasmon, we have fixed the wave vector as $q = 0.0001 \text{ \AA}^{-1}$, which corresponds to a typical micron wavelength easily available in experiments¹⁴.

The collective plasmon mode is defined at zeros of Eq. (3). In general, the dielectric function is a complex functional. The complex solution at $\epsilon(\mathbf{q}, \omega) = 0$ gives both the plasmon dispersion (real part) and the decay of the plasmon (imaginary part). In order to compare with the experiments, it is more convenient to calculate the electron energy loss spectrum (EELS), whose broadened peaks indicate the plasmons²⁸

$$\text{EELS} = -\text{Im}[1/\epsilon(\mathbf{q}, \omega)]. \quad (7)$$

Analytical derivations: In the analytical derivations of ω_p , only the intraband excitations are considered. $E(\mathbf{k}) = \hbar^2 k^2/2m$ and $E(\mathbf{k}) = \hbar v_F k$ are employed for conventional EGs and TSMs, respectively. The overlap form factor is $F(\mathbf{k}, \mathbf{q}) = 1$, and a Fermi-Dirac distribution function with 0 K is adopted. The detailed derivations for all systems are shown in Supplementary Information. The final results are summarized in the right column of Table 1. In comparison with the results of numerical calculations, the degeneracy factor g should be adopted as 4 for Cu₂Si, CuSe and AgTe, because of the two nodal lines in these three TSMs, 4 (6) for double-walled nanotubes (triple-walled

nanotubes), and 2 for other materials.

Calculations of plasmon lifetime

The phonon-assisted damping rate of plasmons is only considered, due to the forbidden or weak direct Landau damping in the studied systems at long-wavelength limit. The plasmon lifetime can be determined from the ac conductivity, which is related to the transport relaxation time (τ_{tr})⁵⁰. The transport scattering rate can be written as⁵⁰

$$\frac{1}{\tau_{tr}} = \frac{2\pi}{\omega} \int_0^\omega d\omega' (\omega - \omega') \alpha_{tr}^2 F(\omega'). \quad (8)$$

$\alpha_{tr}^2 F$ is transport-related Eliashberg spectral function and it is defined as

$$\alpha_{tr}^2 F(\omega) = \frac{1}{2N_F} \sum_{\mathbf{k}q\nu} |g^\nu(\mathbf{k}, \mathbf{q})|^2 \left(-\frac{q \cdot \mathbf{k}}{k^2}\right) \delta(\varepsilon_{\mathbf{k}} - \varepsilon_F) \delta(\varepsilon_{\mathbf{k}+\mathbf{q}} - \varepsilon_F) \delta(\omega - \omega_{\nu q}), \quad (9)$$

where $g^\nu(\mathbf{k}, \mathbf{q})$ is the electron-phonon (*e-ph*) matrix element. It quantifies a scattering process from an initial Bloch state $|n\mathbf{k}\rangle$ (with band n and momentum \mathbf{k}) to a final state $|m\mathbf{k} + \mathbf{q}\rangle$ by emitting or absorbing a phonon with wavevector \mathbf{q} , mode index ν and frequency $\omega_{\nu q}$,

$$g_{nm\nu}(\mathbf{k}, \mathbf{q}) = \frac{1}{\sqrt{2\omega_{\nu q}}} \langle m\mathbf{k} + \mathbf{q} | \partial_{q\nu} V | n\mathbf{k} \rangle, \quad (10)$$

where $\partial_{q\nu} V$ is the derivative of the self-consistent potential.

The *e-ph* coupling matrix elements can be computed within the density-functional perturbation theory (DFPT). Here, a Wannier-Fourier interpolation method as implemented in the EPW code⁵¹ and integrated in the Quantum ESPRESSO package⁵² is used to obtain the numerical results of *e-ph* coupling. The electron eigenstates and eigenvalues, vibrational modes and frequencies, as well as *e-ph* matrix elements are first calculated on a relatively coarse BZ grid, and then Wannier-interpolated values on a fine grid are obtained.

References

1. Tonouchi, M. Cutting-edge terahertz technology. *Nat. Photon.* **1**, 97–105 (2007).
2. Saeedkia, D. *Handbook of terahertz technology for imaging, sensing and communications* (Woodhead Publishing Limited, Cambridge, UK, 2013).
3. Maier, S. A. *Plasmonics: Fundamentals and Applications* (Springer, New York, 2007).
4. Barnes, W. L., Dereux, A. & Ebbesen, T. W. Surface plasmon subwavelength optics. *Nature* **424**, 824–830 (2003).
5. Chen, H.-T. *et al.* Active terahertz metamaterial devices. *Nature* **444**, 597–600 (2006).
6. Zheludev, N. I. & Kivshar, Y. S. From metamaterials to metadevices. *Nat. Mater.* **11**, 917–924 (2012).
7. Yu, N. *et al.* Terahertz plasmonics. *Electron. Lett.* **46**, S52–S57 (2010).
8. Zhang, X. *et al.* Terahertz surface plasmonic waves: a review. *Adv. Photon.* **2**, 014001 (2020).
9. Pendry, J. B., Martín-Moreno, L. & García-Vidal, F. J. Mimicking Surface Plasmons with Structured Surfaces. *Science* **305**, 847–848 (2004).
10. Williams, C. R. *et al.* Highly confined guiding of terahertz surface plasmon polaritons on structured metal surfaces. *Nat. Photon.* **2**, 175–179 (2008).
11. Allen, S. J., Tsui, D. C. & Logan, R. A. Observation of the two-dimensional plasmon in silicon inversion layers. *Phys. Rev. Lett.* **38**, 980–983 (1977).

12. Dyer, G. C. *et al.* Induced transparency by coupling of Tamm and defect states in tunable terahertz plasmonic crystals. *Nat. Photon.* **7**, 925–930 (2013).
13. Kriegel, I., Scotognella, F. & Manna, L. Plasmonic doped semiconductor nanocrystals: Properties, fabrication, applications and perspectives. *Phys. Rep.* **674**, 1–52 (2017).
14. Ju, L. *et al.* Graphene plasmonics for tunable terahertz metamaterials. *Nat. Nanotech.* **6**, 630–634 (2011).
15. Grigorenko, A. N., Polini, M. & Novoselov, K. S. Graphene plasmonics. *Nat. Photon.* **6**, 749–758 (2012).
16. Ni, G. X. *et al.* Fundamental limits to graphene plasmonics. *Nature* **557**, 530–533 (2018).
17. Luther, J. M., Jain, P. K., Ewers, T. & Alivisatos, A. P. Localized surface plasmon resonances arising from free carriers in doped quantum dots. *Nat. Mater.* **10**, 361–366 (2011).
18. Bandurin, D. A. *et al.* Resonant terahertz detection using graphene plasmons. *Nat. Commun.* **9**, 5392 (2018).
19. Muravjov, A. V. *et al.* Temperature dependence of plasmonic terahertz absorption in grating-gate gallium-nitride transistor structures. *Appl. Phys. Lett.* **96**, 042105 (2010).
20. Tantiwanichapan, K. *et al.* Graphene Terahertz Plasmons: A Combined Transmission Spectroscopy and Raman Microscopy Study. *ACS Photonics* **4**, 2011–2017 (2017).
21. Hendry, E. *et al.* Optical control over surface plasmon polariton-assisted THz transmission through a slit aperture. *Phys. Rev. Lett.* **100**, 123901 (2008).
22. Ju, L. *et al.* Photoinduced doping in heterostructures of graphene and boron nitride. *Nat. Nanotech.* **9**, 348–352 (2014).
23. Ni, G. X. *et al.* Ultrafast optical switching of infrared plasmon polaritons in high-mobility graphene. *Nat. Photon.* **10**, 244–247 (2016).
24. Burkov, A. A., Hook, M. D. & Balents, L. Topological nodal semimetals. *Phys. Rev. B* **84**, 235126 (2011).
25. Armitage, N. P., Mele, E. J. & Vishwanath, A. Weyl and Dirac semimetals in three-dimensional solids. *Rev. Mod. Phys.* **90**, 015001 (2018).
26. Sarma, S. D. & Hwang, E. H. Collective modes of the massless Dirac plasma. *Phys. Rev. Lett.* **102**, 206412 (2009).
27. Shi, Z. *et al.* Observation of a Luttinger-liquid plasmon in metallic single-walled carbon nanotubes. *Nat. Photon.* **9**, 515–519 (2015).
28. Wang, J. *et al.* Anomalous Dirac Plasmons in 1D Topological Electrides. *Phys. Rev. Lett.* **123**, 206402 (2019).
29. Wang, J. *et al.* Pseudo Dirac nodal sphere semimetal. *Phys. Rev. B* **98**, 201112(R) (2018).
30. Wixforth, A., Sundaram, M., Ensslin, K., English, J. H. & Gossard, A. C. Dimensional resonances in wide parabolic quantum wells. *Phys. Rev. B* **43**, 10000(R) (1991).
31. Wang, Y., Plummer, E. W. & Kempa, K. Foundations of Plasmonics. *Advances in Physics* **60**, 799–898 (2011).
32. Voit, J. One-dimensional Fermi liquids. *Rep. Prog. Phys.* **58**, 977–1116 (1995).
33. Gao, L. *et al.* Epitaxial Growth of Honeycomb Monolayer CuSe with Dirac Nodal Line Fermions. *Adv. Mater.* **30**, 1707055 (2018).
34. Liu, B. *et al.* Flat AgTe Honeycomb Monolayer on Ag(111). *J. Phys. Chem. Lett.* **10**, 1866–1871 (2019).
35. Zhong, C. *et al.* Two-dimensional honeycomb borophene oxide: strong anisotropy and nodal

- loop transformation. *Nanoscale* **11**, 2468–2475 (2019).
36. Lu, J. L. *et al.* Two-Dimensional Node-Line Semimetals in a Honeycomb-Kagome Lattice. *Chin. Rev. Lett.* **34**, 057302 (2017).
37. Feng, B. *et al.* Experimental realization of two-dimensional Dirac nodal line fermions in monolayer Cu₂Si. *Nat. Commun.* **8**, 1007 (2017).
38. Yang, B., Zhang, X. & Zhao, M. Dirac node lines in two-dimensional Lieb lattices. *Nanoscale* **9**, 8740–8746 (2017).
39. Niu, C. *et al.* Two-dimensional topological nodal line semimetal in layered X₂Y (X=Ca, Sr, and Ba; Y=As, Sb, and Bi). *Phys. Rev. B* **95**, 235138 (2017).
40. Yan, H. *et al.* Damping pathways of mid-infrared plasmons in graphene nanostructures. *Nat. Photon.* **7**, 394–399 (2013).
41. Geim, A. K. & Grigorieva, I. V. Van der Waals heterostructures. *Nature* **499**, 419–425 (2013).
42. Novoselov, K. S., Mishchenko, A., Carvalho, A. & Castro Neto, A. H. 2D materials and van der Waals heterostructures. *Science* **353**, aac9439 (2016).
43. Hamada, N., Sawada, S. & Oshiyama, A. New one-dimensional conductors: Graphitic microtubules. *Phys. Rev. Lett.* **68**, 1579 (1992).
44. Wang, S. *et al.* Logarithm Diameter Scaling and Carrier Density Independence of One-Dimensional Luttinger Liquid Plasmon. *Nano Lett.* **19**, 2360–2365 (2019).
45. Saito, R., Dresselhaus, G. & Dresselhaus, M. S. *Physical Properties of Carbon Nanotubes* (Imperial College Press, London, 1998).
46. Kresse, G. & Furthmüller, J. Efficient iterative schemes for ab initio total-energy calculations using a plane-wave basis set. *Phys. Rev. B* **54**, 11169 (1996).
47. Blöchl, P. E. Projector augmented-wave method. *Phys. Rev. B* **50**, 17953 (1994).
48. Perdew, J. P., Burke, K. & Ernzerhof, M. Generalized Gradient Approximation Made Simple. *Phys. Rev. Lett.* **77**, 3865 (1996).
49. Souza, I., Marzari, N. & Vanderbilt, D. Maximally localized Wannier functions for entangled energy bands. *Phys. Rev. B* **65**, 035109 (2001).
50. Mahan, G. D. *Many-Particle Physics* (Plenum Press, New York, 1990).
51. Poncé, S., Margine, E. R., Verdi, C. & Giustino, F. EPW: Electron–phonon coupling, transport and superconducting properties using maximally localized Wannier functions. *Comput. Phys. Comm.* **209**, 116–133 (2016).
52. Giannozzi, P. *et al.* QUANTUM ESPRESSO: a modular and open-source software project for quantum simulations of materials. *J. Phys.: Condens. Matter* **21**, 395502 (2009).

Acknowledgements

The authors thank L. Kang for helpful discussions. J.W. and B.H. acknowledge the support from Science Challenge Project TZ2016003 and NSAF U1930402. X.S. and W.D. acknowledge support from MOST of China (Grant No. 2016YFA0301001), NSFC (Grants No. 11674188 and No. 11874035) and the Beijing Advanced Innovation Center for Future Chip (ICFC). F.L. acknowledge the support from US-DOE (Grant No. DE-FG02-04ER46148). Part of the calculations were performed at Tianhe2-JK at CSRC.

Author contributions

B.H. and J.W. conceived the project. B.H. supervised the project. J.W. derived the forms of plasmon frequencies. J.W. and X.S. performed DFT, plasmon and lifetime calculations. J.W. and B.H. wrote the paper. All authors contributed to the analyses and discussions of results.